nature nanotechnology

Article

https://doi.org/10.1038/s41565-023-01380-9

Spin-dependent properties of optical modes guided by adiabatic trapping potentials in photonic Dirac metasurfaces

Received: 7 April 2022

Accepted: 20 March 2023

Published online: 27 April 2023



Svetlana Kiriushechkina © ^{1,4}, Anton Vakulenko ® ^{1,4}, Daria Smirnova © ^{2,4}, Sriram Guddala ® ¹, Yuma Kawaguchi ¹, Filipp Komissarenko ¹, Monica Allen ³, Jeffery Allen ³ & Alexander B. Khanikaev ® ¹ ⊠

The Dirac-like dispersion in photonic systems makes it possible to mimic the dispersion of relativistic spin-1/2 particles, which led to the development of the concept of photonic topological insulators. Despite recent demonstrations of various topological photonic phases, the full potential offered by Dirac photonic systems, specifically their ability to emulate the spin degree of freedom-referred to as pseudo-spin-beyond topological boundary modes has remained underexplored. Here we demonstrate that photonic Dirac metasurfaces with smooth one-dimensional trapping gauge potentials serve as effective waveguides with modes carrying pseudo-spin. We show that spatially varying gauge potentials act unevenly on the two pseudo-spins due to their different field distributions, which enables control of guided modes by their spin, a property that is unattainable with conventional optical waveguides. Silicon nanophotonic metasurfaces are used to experimentally confirm the properties of these guided modes and reveal their distinct spin-dependent radiative character; modes of opposite pseudo-spin exhibit disparate radiative lifetimes and couple differently to incident light. The spin-dependent field distributions and radiative lifetimes of their guided modes indicate that photonic Dirac metasurfaces could be used for spin-multiplexing, controlling the characteristics of optical guided modes, and tuning light-matter interactions with photonic pseudo-spins.

Recent progress in subwavelength nanopatterning of optical materials has enabled designer photonic systems that can emulate diverse and exciting physical phenomena ^{1,2}. Photonic structures with Dirac-like conical dispersion represent one class of artificial optical materials and have led to the prediction and observation of unconventional modes in photonic graphene ³, weak antilocalization ^{4,5}, topological phenomena ^{6–13}, and novel non-Hermitian ^{14–20} and nonlinear ^{21–27} physics.

The Dirac-like dispersion is realized in photonic structures with additional lattice symmetries introduced into their design. Thus, hexagonal symmetry of a lattice enables diabolic Dirac points near two (K and K') high-symmetry points of the Brillouin zone. In two dimensions, this enables valley physics in photonic modes exhibiting spinless Dirac-like dispersion 3,28,29 . The Dirac points play the role of magnetic monopoles in momentum space and give rise to a range of

¹Electrical Engineering and Physics, The City College of New York, New York, NY, USA. ²ARC Centre of Excellence for Transformative Meta-Optical Systems (TMOS), Research School of Physics, The Australian National University, Canberra, ACT, Australia. ³Air Force Research Laboratory, Munitions Directorate, Eglin AFB, Eglin, FL, USA. ⁴These authors contributed equally: Svetlana Kiriushechkina, Anton Vakulenko, Daria Smirnova.

©e-mail: akhanikaev@ccny.cuny.edu

topological phenomena 10,30-32. To mimic a 'spin-full' Dirac physics that is characterized by the double degeneracy of bands, the pseudo-spin degree of freedom must be added either by introduction of additional symmetries 33-35 or by folding the valleys onto one another by lattice perturbations 36-39. This brings modes originally residing below the light cone to the new position above the light cone and makes them radiative 38, with stronger perturbation yielding stronger radiative leakage of the modes.

In this Article, we demonstrate that the spin-full nature of Dirac photonic structures can be leveraged to create photonic systems that can trap and guide optical modes with an additional degree of control enabled by pseudo-spin. Synthetic gauge potentials produced by non-uniform nanopatterning allow generation of spin-dependent field distributions and radiative properties of guided modes.

Theoretical model

We consider a photonic system described by a spin-full effective Dirac Hamiltonian of the form:

$$\hat{H}(\mathbf{r}) = \hat{\sigma}_z \hat{s}_0 m(\mathbf{r}) - i\hat{\sigma}_x \hat{s}_z \partial_x - i\hat{\sigma}_y \hat{s}_0 \partial_y, \tag{1}$$

where $\mathbf{r} = (x,y)$ is the two-dimensional radius vector, \hat{s}_i , $\hat{\sigma}_i$ are Pauli matrices for the pseudo-spin and sublattice degrees of freedom, respectively, and $m(\mathbf{r})$ is the position-dependent mass term. The Hamiltonian (1) can be obtained directly from either the tight-binding model³⁶ or the plane wave expansion³⁹ of the crystal systems it describes. Importantly, the spin degree of freedom in equation (1) is generated by the fermionic-type pseudo-time-reversal symmetry $\mathcal{T}^2 = -1$, where $\mathcal{T} = -i\sigma_{\nu}K$, and K is complex conjugation. As can be shown from the group-theoretical analysis, the presence of this symmetry in turn is ensured by the rotational C_6 symmetry of the physical system⁴⁰. The spin-full waveguide is created by a non-uniform mass term m(x), and the trapping 'potential' in the x direction is formed when a 'guiding' region of smaller mass (compared to the 'cladding' region $|m_g(x)| < |m_c|$) is present. Thus, a simple waveguide can be constructed by choosing a square-well-shaped mass term, where the confinement mechanism due to the wider bandgap for the cladding region is the most evident. Assuming the eigenstates of the Hamiltonian (1) in the form of guided modes, $|\psi(r)\rangle = u(x) \exp(i\tilde{k}_{v}y)$, where \tilde{k}_{v} is the wavenumber in the direction of propagation of guided modes (y direction), one can explicitly derive an expression 31 for new (squared in the $\hat{\sigma}_i$ subspace) Hamiltonian $\widehat{\mathcal{H}} = \widehat{H}^2$ of the form:

$$\widehat{\mathcal{H}}\left(\bar{k}_{y}\right) = -\partial_{x}^{2} + \left[\bar{k}_{y}^{2} + m^{2}\left(x\right)\right] - \hat{\sigma}_{y}\hat{s}_{z}\left[\partial_{x}m\left(x\right)\right]. \tag{2}$$

The second term in this more familiar (Helmholtz-like) form of Hamiltonian equation (2) represents a well-recognizable one-dimensional 'potential well' for the guided modes in the waveguide and does not depend on the pseudo-spin of the mode. However, the third term clearly introduces such dependence showing the pseudo-spin-dependent form of the eigenmodes described by the Hamiltonians (1) and (2).

The spin-full nature of such 'Dirac waveguides' and the ability to generate spin-dependent trapping potentials with carefully designed inhomogeneous distributions of the mass term expands opportunities to control light. For example, one can envision 'spintronics for light' with spin-polarized photons in Dirac waveguides analogous to similar physics demonstrated for electrons in solids. One difference from electronic systems stems from the very nature of light and its ability to couple and leak into the radiative continuum with the related non-Hermitian physics. The spin-dependent potentials lead to distinct modal profiles for two photonic pseudo-spins, giving rise to different radiative properties and lifetimes of modes carrying opposite pseudo-spins. The latter effect reported here is referred to as the non-Hermitian spin Hall effect.

Because photonic realization assumes the possibility of radiative loss, for the case of Dirac bands located above the light line, we need to prescribe the modes' radiative characteristics by assigning them a radiative lifetime or related radiative propagation length. By analogy to the leaky modes in nanostructured topological metasurfaces 36,39,41 , the spinor functions of the bands can be assigned dipolar and quadrupolar components, and it is only the dipolar component that leads to radiation into the far-field. This allows us to calculate the complex-valued spectrum of the modes, $\gamma_R \equiv \text{Im}(\omega)$, where γ_R is the radiative damping coefficient, by using the solutions of the Dirac equation with the radiative leakage considered as perturbation (Supplementary Information, section 1).

We first analyse solutions of the Dirac equation (1) with non-uniform but symmetric distribution of the mass term (shown in subplot Fig. 1a, the top panel) to illustrate emergent properties enabled by the spin-full nature of the system. The mechanism of mode confinement by this potential is clear and stems from the narrower photonic bandgap in the centre of the structure compared to a broader bandgap on the sides (that is, in the cladding). The Dirac eigenvalue problem for the quadratic potential well is solved numerically by applying the Susskind discretization scheme 42,43. Our calculations confirm that the band structure (shown in Fig. 1a, the bottom panel) contains additional bands separated from the gapped continuum when compared to the case of the uniform mass term. These bands are doubly degenerate with respect to the pseudo-spin, obey particle-hole symmetry and thus appear at both positive and negative energies. The field profiles of these additional bands confirm that the modes are indeed localized in the trapping region of lower mass and the solutions have perfectly degenerate spectra for the two pseudo-spins. It is interesting that the field profiles exhibit a spin Hall effect-like behaviour with the centre of localization being shifted away from the centre of the trapping region (x = 0) in positive or negative direction, depending on the pseudo-spin value. From the symmetry of the trapping potential, it follows that the two solutions corresponding to two pseudo-spins transform into one another under the reflection $(x \rightarrow -x)$. Calculations show that the spatially symmetric profile makes it possible to minimize the spin dependence. Indeed, the damping coefficient (shown by the colour of the bands in Fig. 1) appears to be identical for the two pseudo-spins $\gamma_R^{\uparrow} = \gamma_R^{\downarrow}$.

Next, we consider an antisymmetric distribution of the mass term. The results for the analytically solvable kink profile $m(x) = \tanh(x/w)$, corresponding to the Pöschl–Teller-like trapping potential 31,44 in the Schrödinger-like equation with Hamiltonian (2), are shown in Fig. 1b. Details about the analytical solution for this case are provided in Supplementary Information, section 1. The spectrum of bound states is

given by $\omega_n=\pm\sqrt{\hat{k}_y^2+1-(1-n/w)^2}$, where n=0,1,2,...,[w]. Similar to the symmetric case, we observe doubly degenerate solutions that correspond to the two pseudo-spins at both positive and negative energies. In the antisymmetric case, however, the field profiles show completely different field distributions, confirming that the two pseudo-spins perceive different effective trapping potentials. Insets to the band structure plot in Fig. 1b show profiles for the two pseudo-spins with two specific values of momenta, $\tilde{k}_y>0$ and its time-reversal partner $-\tilde{k}_y$, for both positive and negative energies. The profiles are noticeably different for the two different pseudo-spins, with the maximum in the centre for the spin-up state $|\psi^{\dagger}\rangle$ instead of the minimum for the spin-down $|\psi^{\dagger}\rangle$ state for $\tilde{k}_y>0$. As expected from the time-reversal and particle—hole symmetries of this system, reversal of either the momentum or the sign of the energy leads to flipping of the field profiles for the two pseudo-spins.

We note that in the case of an antisymmetric trapping profile, the mass term inversion leads to the formation of a topological domain wall that supports topological edge states with linear-like dispersion. These modes are known to be one-way spin-polarized with dispersion $\omega_{\downarrow,\uparrow} \approx \pm |\nu_{\rm g}| \tilde{k}_{\nu}$, where plus and minus signs correspond to two opposite

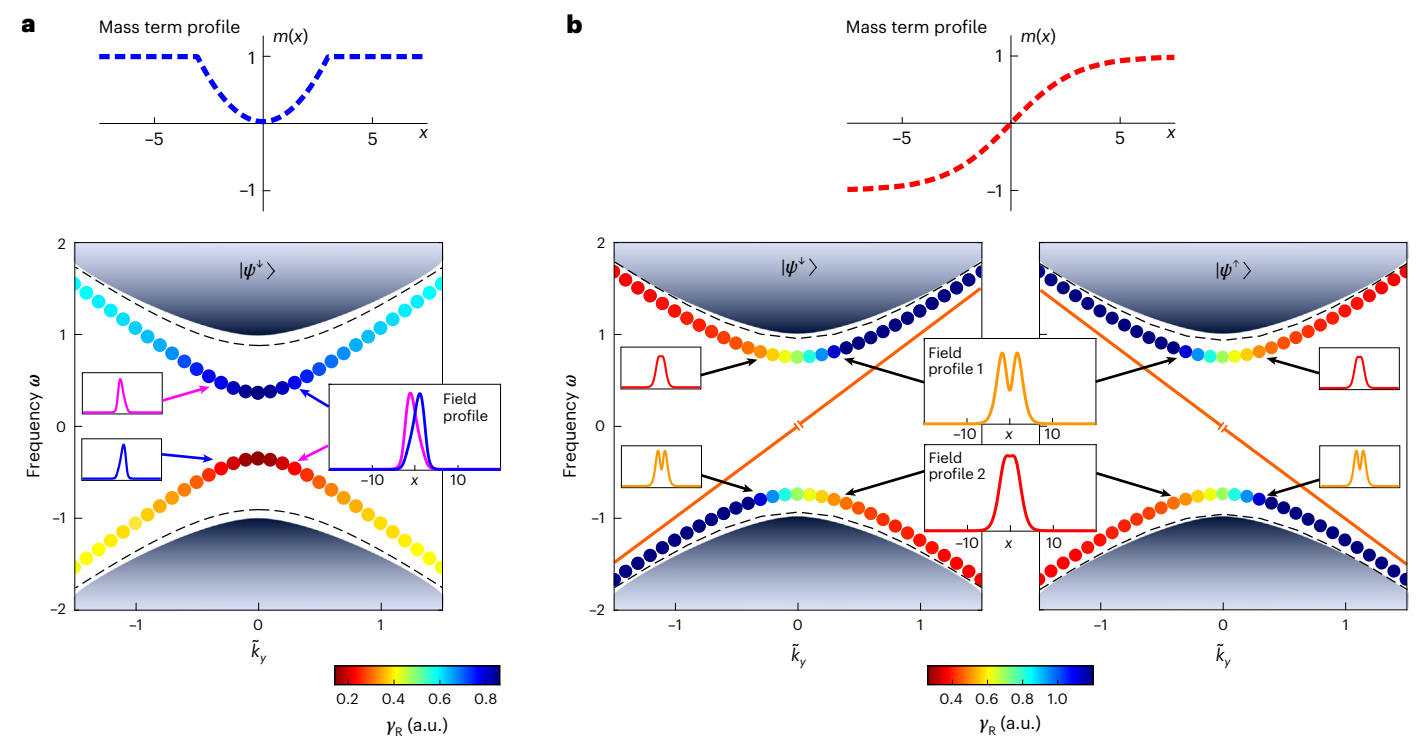


Fig. 1|**Spin-full guiding potentials generated by spatially variable mass terms. a**, Top: symmetric mass term with parabolic shape in the centre of the spin-full waveguide $m(x) = (x/w)^2$ of width w = 3; bottom: corresponding spectrum of four doubly degenerate lowest-energy spin-full guided modes (dotted line), four similar higher-energy states (dashed lines) and bulk continuum modes. The spectra of the two pseudo-spins are doubly degenerate in both real and imaginary parts, and therefore only one spin is shown. The radiative damping coefficient of the modes is colour-coded and breaks the particle-hole symmetry of the spectrum. The field profiles (i.e., $\psi^{\uparrow\downarrow}$) for different energy/

frequency and momenta are shown as insets. **b**, Top: antisymmetric mass term $m(x) = \tanh(x/w)$ corresponding to the Pöschl–Teller trapping potential; bottom: corresponding energy/frequency spectra of the spin-polarized guided modes trapped near the centre (x=0). The two spins have different radiative lifetimes (non-Hermitian spin Hall effect) colour-coded by the radiative damping coefficient of the modes, and distinct field profiles (1 with and 2 without a pronounced minimum in the middle shown in insets) due to the spin-dependent character of the waveguide. a.u., arbitrary unit.

 $(\downarrow$ and $\uparrow)$ spins, and $\nu_{\rm g}$ is the group velocity 37,45 . As such, while these modes have unique properties of topological robustness, they are necessarily not spin-full and do not allow propagation of the opposite spins in the same direction. Thus, these modes should be contrasted with our guided modes originating not from the reversal of the mass term, but from its smooth variation, indicating a different confinement mechanism. As a result, the guided modes reported here can exist even without reversal of the mass term, and, while not exhibiting any topological resilience, they offer spin-full propagation along the waveguides produced by the variation of the mass term.

Another important observation that can be made from our calculation results in Fig. 1b is that, despite different field distributions, the modes guided by the Dirac waveguide retain their spin degeneracy in the real part of the spectrum. The radiative nature of the modes, however, implies that different field profiles will have a dramatic effect on the imaginary part of the spectra. Indeed, the modes switch between predominantly dipolar (radiative) and predominantly quadrupolar (non-radiative) across the centre of antisymmetric trapping potential due to the band inversion mechanism, which gives rise to the strong sensitivity of the radiative properties of the guided modes to their field distributions. The calculations of the radiative damping coefficient of the modes, shown in colour in Fig. 1b, indeed confirm strong spin-dependent radiative properties and corroborate the non-Hermitian spin Hall effect.

First-principles studies

We chose a leaky silicon photonic crystal (metasurface) design^{37,38} with a pseudo-spin-degenerate Dirac cone at normal incidence (k = 0) to

experimentally verify the predicted mechanism of light trapping and the pseudo-spin-dependent properties of guided modes. The structure represents a lattice with unit cells containing a hexamer of triangles. This lattice structure exhibits a gap that opens when the symmetry of the structure is reduced by shifting triangles either towards (lower inset in Fig. 2a) or away from each other (upper insert in Fig. 2a), giving rise to trivial and topological phases, respectively. This design has been previously used to demonstrate spin Hall-like topological photonic 38,45 and polaritonic boundary modes $^{46-48}$. Here, in contrast, we are specifically interested in spin-full guided modes that can be induced by variation of the mass term in the Dirac Hamiltonian emulated by this system.

The rotational C₆ symmetry of the lattice of this metasurface endows its modes with orbital momentum L_z . Following ref. 49, this quantity can be directly evaluated from the field profiles obtained by first-principles numerical studies, which confirm that the dipolar modes carry total angular momentum $J_z = L_z + S_z = \pm 1$. We note that J_z is the quantity that represents the pseudo-spin of our modes. The total value of J_z should remain unchanged as we move from the near-field to the far-field of the structure, but it is dominated by the spin in the far-field $(J_z \rightarrow S_z)$ where evanescent components vanish. This asymptotic far-field behaviour enables selective excitation of the two pseudo-spins by circularly left $(S_z = -1)$ and circularly right $(S_z = -1)$ polarized waves incident near-normally onto the structure. In the near-field, in contrast, J_z is dominated by the orbital momentum L_z , and the spin component S_z is less than 7%. We note that a similar conversion of spin-to-orbital angular momentum has been previously reported in a different but related context in ref. 50. We also note that for large angles of incidence

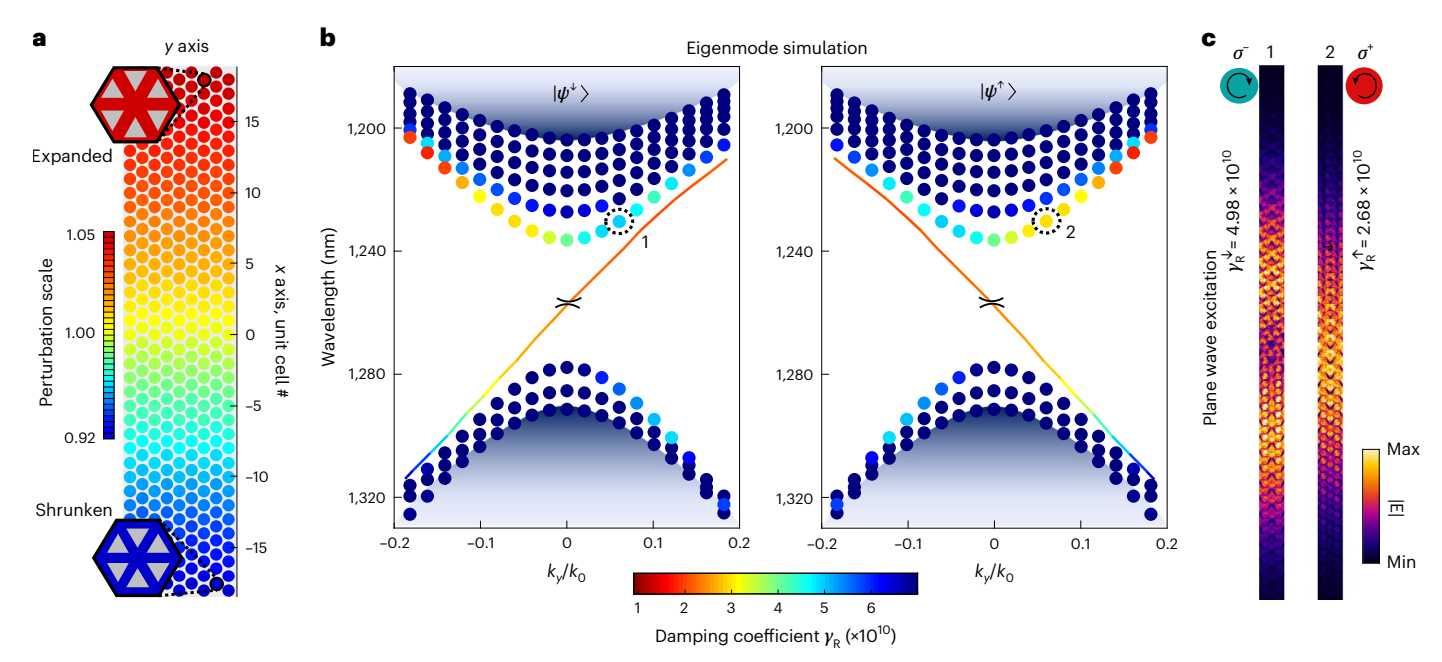


Fig. 2 | **First-principles design of a spin-full waveguide and non-Hermitian spin Hall effect. a**, A Dirac metasurface with variable lattice perturbation gives rise to the position-dependent effective mass term. The geometry of the resultant Dirac meta-waveguide changes from shrunken at the bottom to expanded at the top. The colour bar shows the degree of perturbation from an ideal graphene-like lattice ³⁷. **b**, Complex eigenfrequency spectra of pseudo-spin-up $(J_z = 1)$ and pseudo-spin-down $(J_z = -1)$ modes with lifetimes colour-coded as damping coefficient γ_R . Separation of spectra into two pseudo-spins was performed by direct calculation of the angular momentum $(J_z = 1)$ for spin-up

and $J_z = -1$ for spin-down) from the fields obtained in first-principles (finite-element method) studies. The edge state spectrum is shown as a continuous line with a small gap as indicated. \mathbf{c} , Field distributions for Dirac waveguide modes excited by circularly polarized light of opposite helicities (σ^t) calculated for the same wavelength and momentum corresponding to the positions in the eigenfrequency spectra denoted by circles 1 and 2. The spin-dependent field distribution and the resultant difference in the radiative lifetimes (damping coefficients in \mathbf{b}) of the modes highlight the non-Hermitian spin Hall effect.

the pseudo-spin will break down due to the 'extrinsic' reduction of symmetry caused by large values of the Bloch momentum 51,52 . This reduction of symmetries can be accounted for by an effective spin-mixing due to the terms nonlinear in Bloch momentum 39 . Thus, in the continuum model equation (1) the spin-mixing is introduced by adding the 2×2 pseudo-spin sectors $\widehat{H}_{\uparrow\downarrow}$ via off-diagonal 2×2 matrices diag $\left\{A\left(k_x+ik_y\right)^2,-A\left(k_x-ik_y\right)^2\right\}$. Our analysis based on fitting the first-principles data to this analytical model yields a value of the parameter $A=0.5\,\mathrm{s}^{-1}$, corresponding to -5% energy correction even for a relatively large value of momentum $\frac{k_y}{k_0}=0.2$, which shows that the spin of the modes remains a well-defined quantity for the range of momenta of interest (Supplementary Information , section 2).

The spin-full waveguide in the metasurfaces is formed by adiabatically varying the distance between the triangles that form the unit cell across one of the directions, as shown in Fig. 2a. This produces a linear mass-term profile that varies from negative to positive for the pseudo-spin-up $|\psi^{\dagger}\rangle$ states, and positive to negative for the pseudo-spin-down $|\psi^{\downarrow}\rangle$ states. It is known that the two perturbations, shrinkage and expansion, respectively, yield different widths of the bandgap for the same degree of geometric perturbation (measured by the shift of the triangles), and yield different effective mass terms 37 . Therefore, the degree of perturbation as a function of the position across the waveguide has to be tuned to provide similar confinement in the regions of positive and negative mass term, which is reflected in the asymmetry of geometric perturbation in Fig. 2a (5% for expanded and 8% for shrunken).

Our first-principles numerical simulations (Fig. 2b) confirm the formation of spin-degenerate guided eigenmodes that split from the bulk continuum. The field profiles of these states show that they indeed are trapped by the effective potential produced by the mass-term variation. The profiles for pseudo-spin-up $|\psi^{\dagger}\rangle$ and pseudo-spin-down $|\psi^{\downarrow}\rangle$

states of the same frequency and momentum, which correspond to the lowest energy states, are plotted in Fig. 2c. These profiles clearly highlight differences in the field distribution and confirm the spin-dependent character of the effective potential confining these modes. More importantly, our first-principles calculations confirm distinct field distributions of the modes with opposite pseudo-spin, which gives rise to the non-Hermitian spin Hall effect with spin-up and spin-down modes having different radiative damping.

Experimental observation of pseudo-spin-dependent properties of guided modes

The presence of spin-full guided modes and the non-Hermitian spin Hall effect was experimentally confirmed for a 220-nm-thick silicon on insulator nanostructure with a variable lattice perturbation shown in Fig. 2a. The spectrum and propagation of the modes of the Dirac waveguide were probed by a custom-built microscope system that can image a sample in real and Fourier domains in the reflection geometry. To reveal the spin-dependent non-Hermitian physics of the structure, we utilized the circularly polarized nature of the far-field component of the modes and performed direct selective excitation of the pseudo-spin-polarized guided modes using circularly polarized light focused on the centre of the Dirac waveguide \$3-55 (see Methods for details on fabrication and experiment).

First, real-space images of the modes (Fig. 3b) excited by left-circularly (σ^+ , S = +1) and right-circularly polarized (σ^- , S = -1) light of the same intensity and momentum (a specific wavenumber k_y was spatially filtered with an aperture) were obtained and confirmed excitation of the guided modes and their spatial confinement. The evident difference in the brightness of the two guided modes for the same excitation intensity confirms the different radiative properties of the

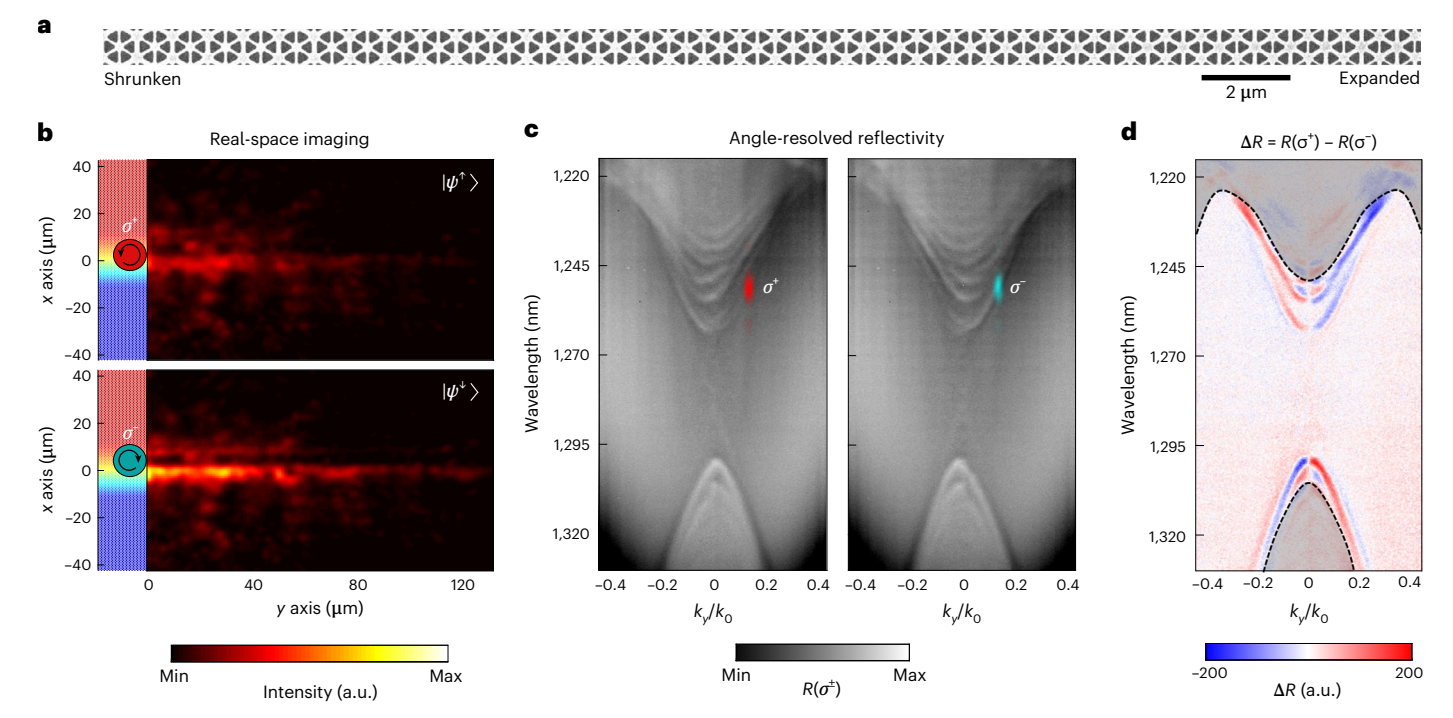


Fig. 3 | **Experimental results evidencing pseudo-spin-polarized transport and non-Hermitian spin Hall effect in the Dirac meta-waveguide. a**, Scanning electron microscopy image of a cross-section of the Dirac meta-waveguide with antisymmetric mass term distribution and zero mass at the centre. **b**, Real-space images of the spectrally and momentum-space filtered excitations of the lowest upper-frequency (positive energy) guided modes of the Dirac meta-waveguide, driven by left (σ^*) and right (σ^-) circularly polarized light for selective excitation of pseudo-spin-up and pseudo-spin-down modes, respectively. **c**, Momentum-space (Fourier-plane) images of the Dirac meta-waveguide in the reflection geometry

with circular left and right excitation (left and right panels, respectively) showing dispersion of the guided and bulk pseudo-spin-up and pseudo-spin-down modes. The greyscale reflectivity maps are overlayed by coloured data (red and cyan) which show positions of spectral and momentum filtering of the excitation beam (labelled as σ^+ and σ^- , respectively) for the real-space image in ${\bf b.d.}$, Differential reflectivity spectra evidencing contrast in excitation and leakage of the guided modes of opposite pseudo-spins. Grey shaded regions indicate bulk bands. A comparison with the results for the symmetric Dirac meta-waveguide is provided in Supplementary Fig. 3. a.u., arbitrary unit.

modes. Even more evident difference in the radiative properties of the modes of opposite pseudo-spin was obtained via Fourier-plane (momentum-space) imaging of the nanostructure with circularly polarized excitations, which allowed us to reconstruct its pseudo-spin-dependent photonic band structure. The top and bottom panels in Fig. 3c reveal a clear contrast in the visibility of the reflectivity spectra of the guided modes of two opposite pseudo-spins due to their different radiative properties $\gamma^{\uparrow}(k_y) \neq \gamma^{\downarrow}(k_y)$ for any $k_y \neq 0$, and to asymmetry with respect to the wavenumber inversion $\gamma^{\uparrow}(k_y) \neq \gamma^{\uparrow}(-k_y)$. Analysis based on coupled-mode theory shows that a difference in the reflectivities collected for the two oppositely circularly polarized excitations (the differential reflectivity) $\Delta R = R^{\uparrow} - R^{\downarrow}$, is directly proportional to the difference between damping coefficients $\Delta R \approx \gamma^{\uparrow} - \gamma^{\downarrow} = \Delta \gamma$ (Supplementary Information, section 3). This quantity thus allows to directly quantify the non-Hermitian spin Hall effect.

First, we note that no such spin dependence was observed for guided modes of the symmetric waveguide (Supplementary Information, section 4), and some contrast was seen only in the very close proximity to the bulk modes, which can be attributed to the spin mixing for larger values of the Bloch momentum k. In contrast, for the case of antisymmetric structure, the differential reflectivity spectrum $\Delta R(k_y)$ for the guided modes, shown in Fig. 3d, is highly pronounced with extremes corresponding to the spectral position of the modes. Thus, the observed large values of $\Delta R \approx \Delta \gamma$ in Fig. 3d prove different radiative properties of the oppositely pseudo-spin-polarized modes and the non-Hermitian spin Hall effect.

Conclusions

In this Article, we propose and demonstrate spin-full photonic waveguides based on Dirac metasurfaces. The underlying physics of the

metasurface allows emulation of the spin degree of freedom and generation of spin-dependent effective trapping potentials. We show through theoretical analysis and experimental measurements that a variation of the effective mass term in the Dirac metasurface allows trapping and guiding of pseudo-spin-degenerate guided modes. We predict that inhomogeneous mass terms give rise to distinct field distributions of the modes with opposite pseudo-spins. With a leaky metasurface, the distinct field distributions yield different radiative lifetimes of pseudo-spin-polarized modes—a non-Hermitian spin Hall effect of light, which was confirmed by spin-selective Fourier-plane imaging.

To emphasize the versatility of the proposed trapping mechanism for Dirac photonic systems, we also added results for two types of valley-Hall structures with antisymmetric trapping potentials based on (1) dimerized photonic graphene^{56,57} and (2) a kagome lattice, which give rise to valley-polarized guided modes (Supplementary Information, sections 5 and 6). These designs are characterized by the guided modes which appear below the light cone, and therefore do not exhibit radiative leakage, which can be useful for devices where propagation over long distances or large quality factors are desirable^{56,58}. Thus, the proposed scheme for pseudo-spin-dependent (including valley-dependent) behaviour can be realized in any type of Dirac photonic system, including bi-anisotropic meta-waveguides^{53–55}.

We anticipate that the spin-full nature of the modes reported here will find uses in on-chip quantum photonic devices where quantum information could be encoded by a photonic pseudo-spin. The spin-dependent field distributions and radiative properties of the modes can also be used for selective control of light–matter interactions on a photonic chip, which could be of interest for polaritonic, active and nonlinear photonic devices.

Online content

Any methods, additional references, Nature Portfolio reporting summaries, source data, extended data, supplementary information, acknowledgements, peer review information; details of author contributions and competing interests; and statements of data and code availability are available at https://doi.org/10.1038/s41565-023-01380-9.

References

- Qiao, W. et al. Toward scalable flexible nanomanufacturing for photonic structures and devices. Adv. Mater. 28, 10353–10380 (2016).
- Li, C. et al. Dielectric metasurfaces: from wavefront shaping to quantum platforms. Prog. Surf. Sci. 95, 100584 (2020).
- 3. Plotnik, Y. et al. Observation of unconventional edge states in 'photonic graphene'. *Nat. Mater.* **13**, 57–62 (2014).
- Bliokh, K. Y. Weak antilocalization of ultrarelativistic fermions. Phys. Lett. A 344, 127–130 (2005).
- Morozov, S. V. et al. Strong suppression of weak localization in graphene. Phys. Rev. Lett. 97, 016801 (2006).
- Lu, L., Joannopoulos, J. D. & Soljačić, M. Topological photonics. Nat. Photonics 8, 821–829 (2014).
- Wang, Z., Chong, Y., Joannopoulos, J. D. & Soljačić, M.
 Observation of unidirectional backscattering-immune topological electromagnetic states. *Nature* 461, 772–775 (2009).
- Hafezi, M., Demler, E. A., Lukin, M. D. & Taylor, J. M. Robust optical delay lines with topological protection. *Nat. Phys.* 7, 907–912 (2011).
- Cheng, X. et al. Robust reconfigurable electromagnetic pathways within a photonic topological insulator. *Nat. Mater.* 15, 542–548 (2016).
- Khanikaev, A. B. & Shvets, G. Two-dimensional topological photonics. Nat. Photonics 11, 763–773 (2017).
- Ozawa, T. et al. Topological photonics. Rev. Mod. Phys. 91, 015006 (2019).
- 12. Slobozhanyuk, A. et al. Three-dimensional all-dielectric photonic topological insulator. *Nat. Photonics* **11**, 130–136 (2017).
- 13. Yang, Y. et al. Realization of a three-dimensional photonic topological insulator. *Nature* **565**, 622–626 (2019).
- Szameit, A., Rechtsman, M. C., Bahat-Treidel, O. & Segev, M. PT-symmetry in honeycomb photonic lattices. *Phys. Rev. A* 84, 021806R (2011).
- Zhen, B. et al. Spawning rings of exceptional points out of Dirac cones. Nature 525, 354–358 (2015).
- Leykam, D., Bliokh, K. Y., Huang, C., Chong, Y. D. & Nori, F. Edge modes, degeneracies, and topological numbers in non-Hermitian systems. *Phys. Rev. Lett.* 118, 040401 (2017).
- Liu, T. et al. Second-order topological phases in non-Hermitian systems. *Phys. Rev. Lett.* 122, 076801 (2019).
- Liu, Y. G. N., Jung, P. S., Parto, M., Christodoulides, D. N. & Khajavikhan, M. Gain-induced topological response via tailored long-range interactions. *Nat. Phys.* 17, 704–709 (2021).
- Xia, S. et al. Nonlinear tuning of PT symmetry and non-Hermitian topological states. Science 372, 72–76 (2021).
- 20. Parto, M., Liu, Y. G. N., Bahari, B., Khajavikhan, M. & Christodoulides, D. N. Non-Hermitian and topological photonics: optics at an exceptional point. *Nanophotonics* **10**, 403–423 (2020).
- Lumer, Y., Plotnik, Y., Rechtsman, M. C. & Segev, M. Self-localized states in photonic topological insulators. *Phys. Rev. Lett.* 111, 243905 (2013).
- Hadad, Y., Khanikaev, A. B. & Alù, A. Self-induced topological transitions and edge states supported by nonlinear staggered potentials. *Phys. Rev. B* 93, 55112 (2016).
- Leykam, D. & Chong, Y. D. Edge solitons in nonlinear-photonic topological insulators. *Phys. Rev. Lett.* 117, 143901 (2016).

- 24. Hadad, Y., Soric, J. C., Khanikaev, A. B. & Alú, A. Self-induced topological protection in nonlinear circuit arrays. *Nat. Electron.* **1**, 178–182 (2018).
- D'Aguanno, G. et al. Nonlinear topological transitions over a metasurface. Phys. Rev. B 100, 214310 (2019).
- Smirnova, D., Leykam, D., Chong, Y. & Kivshar, Y. Nonlinear topological photonics. *Appl. Phys. Rev.* 7, 021306 (2020).
- Maczewsky, L. J. et al. Nonlinearity-induced photonic topological insulator. Science 370, 701–704 (2020).
- Gao, F. et al. Topologically protected refraction of robust kink states in valley photonic crystals. Nat. Phys. 14, 140–144 (2018).
- Liu, J. W. et al. Valley photonic crystals. Adv. Phys. X 6, 1905546 (2021).
- Haldane, F. D. M. & Raghu, S. Possible realization of directional optical waveguides in photonic crystals with broken time-reversal symmetry. *Phys. Rev. Lett.* **100**, 013904 (2008).
- Raghu, S. & Haldane, F. D. M. Analogs of quantum-Hall-effect edge states in photonic crystals. *Phys. Rev. A* 78, 033834 (2008).
- 32. Rechtsman, M. C. et al. Photonic Floquet topological insulators. *Nature* **496**, 196–200 (2013).
- Khanikaev, A. B. et al. Photonic topological insulators. *Nat. Mater.* 12, 233–239 (2013).
- 34. Silveirinha, M. G. Bulk-edge correspondence for topological photonic continua. *Phys. Rev. B* **94**, 205105 (2016).
- 35. Bisharat, D. J. & Sievenpiper, D. F. Electromagnetic-dual metasurfaces for topological states along a 1D interface. *Laser Photonics Rev.* **13**, 1900126 (2019).
- Wu, L. H. & Hu, X. Scheme for achieving a topological photonic crystal by using dielectric material. *Phys. Rev. Lett.* 114, 223901 (2015).
- 37. Barik, S., Miyake, H., Degottardi, W., Waks, E. & Hafezi, M. Two-dimensionally confined topological edge states in photonic crystals. *New J. Phys.* **18**, 113013 (2016).
- 38. Barik, S. et al. A topological quantum optics interface. *Science* **359**, 666–668 (2018).
- 39. Gorlach, M. A. et al. Far-field probing of leaky topological states in all-dielectric metasurfaces. *Nat. Commun.* **9**, 909 (2018).
- 40. Mei, J., Chen, Z. & Wu, Y. Pseudo-time-reversal symmetry and topological edge states in two-dimensional acoustic crystals. *Sci. Rep.* **6**, 32752 (2016).
- 41. Smirnova, D. et al. Third-harmonic generation in photonic topological metasurfaces. *Phys. Rev. Lett.* **123**, 103901 (2019).
- 42. Tworzydło, J., Groth, C. W. & Beenakker, C. W. J. Finite difference method for transport properties of massless Dirac fermions. *Phys. Rev. B* **78**, 235438 (2008).
- Hernández, A. R. & Lewenkopf, C. H. Finite-difference method for transport of two-dimensional massless Dirac fermions in a ribbon geometry. *Phys. Rev. B* 86, 155439 (2012).
- 44. Landau, L. D. and Lifschitz, E. M. Quantum Mechanics: Non-relativistic Theory (Pergamon, 1977).
- 45. Parappurath, N., Alpeggiani, F., Kuipers, L. & Verhagen, E. Direct observation of topological edge states in silicon photonic crystals: spin, dispersion, and chiral routing. *Sci. Adv.* **6**, eaaw4137 (2020).
- 46. Liu, W. et al. Generation of helical topological exciton–polaritons. *Science* **370**, 600–604 (2020).
- Li, M. et al. Experimental observation of topological Z2 exciton-polaritons in transition metal dichalcogenide monolayers. *Nat. Commun.* 12, 4425 (2021).
- Guddala, S. et al. Topological phonon–polariton funneling in midinfrared metasurfaces. Science 374, 225–227 (2021).

- Bliokh, K. Y., Dressel, J. & Nori, F. Conservation of the spin and orbital angular momenta in electromagnetism. New J. Phys. 16, 093037 (2014).
- Bliokh, K. Y. et al. Spin-to-orbital angular momentum conversion in focusing, scattering, and imaging systems. Opt. Express 19, 26132 (2011).
- De Paz, M. B., Vergniory, M. G., Bercioux, D., Garciá-Etxarri, A. & Bradlyn, B. Engineering fragile topology in photonic crystals: topological quantum chemistry of light. *Phys. Rev. Res.* 1, 032005 (2019).
- De Paz, M. B. et al. Energy density as a probe of band representations in photonic crystals. *J. Phys. Condens. Matter* 34, 314002 (2022).
- Xiao, B. et al. Exciting reflectionless unidirectional edge modes in a reciprocal photonic topological insulator medium. *Phys. Rev. B* 94, 195427 (2016).
- 54. Slobozhanyuk, A. et al. Near-field imaging of spin-locked edge states in all-dielectric topological metasurfaces. *Appl. Phys. Lett.* **114**, 031103 (2019).
- Li, Y. et al. Mode-selective single-dipole excitation and controlled routing of guided waves in a multi-mode topological waveguide. Appl. Phys. Lett. 120, 221702 (2022).

- Shalaev, M. I., Walasik, W., Tsukernik, A., Xu, Y. & Litchinitser, N. M. Robust topologically protected transport in photonic crystals at telecommunication wavelengths. *Nat. Nanotechnol.* 14, 31–34 (2019).
- Collins, M. J., Zhang, F., Bojko, R., Chrostowski, L. & Rechtsman, M. C. Integrated optical Dirac physics via inversion symmetry breaking. *Phys. Rev. A* 94, 063827 (2016).
- 58. Zeng, Y. et al. Electrically pumped topological laser with valley edge modes. *Nature* **578**, 246–250 (2020).

Publisher's note Springer Nature remains neutral with regard to jurisdictional claims in published maps and institutional affiliations.

Springer Nature or its licensor (e.g. a society or other partner) holds exclusive rights to this article under a publishing agreement with the author(s) or other rightsholder(s); author self-archiving of the accepted manuscript version of this article is solely governed by the terms of such publishing agreement and applicable law.

© The Author(s), under exclusive licence to Springer Nature Limited 2023

Methods

Numerical simulations

We used the commercial software COMSOL Multiphysics for the first-principles simulations presented in this work. The nanophotonic metasurface design was implemented in a silicon slab of 220 nm thickness on a glass substrate to yield a bandgap centre at a wavelength of $\lambda \approx 1,250$ nm. The size of the unit cell with a hexamer of triangle-shaped air holes was $a_0 = 680$ nm, and the side of the equilateral triangle was s = 260 nm. The metasurface with an adiabatically changing mass term was simulated using an array of 39 unit cells along the direction of the mass term profile variation aligned with the x axis. The degree of perturbation of the unit cell was linearly changed from the most expanded unit cell with $R = 1.05 \times a_0/3$, where R is the distance between the centre of the unit cell to the centroid of each triangular hole at one edge of the array, to the unperturbed unit cell $(R = a_0/3)$ in the centre, and to the most shrunken unit cell ($R = 0.92 \times a_0/3$) at the opposite end of the array. The periodic boundary conditions were applied in the y-axis direction. All other boundaries were surrounded by perfectly matched layers. In the eigenfrequency spectra, modes were separated by the sign of pseudo-spin, which was calculated as the out-of-plane component of the angular momentum L_z using the expression from ref. 49: $L_z = \frac{1}{2} \text{Im} \left[\varepsilon_0 \tilde{\varepsilon} \left(-r_v \mathbf{E}^* \cdot (\nabla_x) \mathbf{E} + r_x \mathbf{E}^* \cdot (\nabla_y) \mathbf{E} \right) \right]$, where $\tilde{\varepsilon}$ is the relative dielectric permittivity, $\widetilde{\mu}$ is the relative magnetic permeability, $\mathbf{r} = (r_x, r_y)$ is a radius vector and **E** are numerically calculated electric fields (inside the structure and near-field).

Sample fabrication

The designed Dirac meta-waveguide was fabricated on the SOI substrates (220 nm of silicon, 2 μ m of buried oxide layer) by electron beam lithography (Elionix ELS-G100). First, the substrates were spin-coated with e-beam resist ZEP520A-7 approximately 150 nm thick and then baked for 4 min at 180 °C. For efficient charge dissipation a layer of anticharging agent (DisCharge H20x2) 50 nm thick was spin-coated on top of the resist. After e-beam lithography exposure, the anticharging agent was removed by rinsing with deionzied water and the resist was developed in n-amyl acetate at 0 °C for approximately 30 s. Next, the silicon layer of the exposed area was vertically etched to a depth of 220 nm by inductively coupled plasma in an Oxford PlasmaPro System. The etching recipe is based on C_4F_8/SF_6 gases and achieves an etching rate of about 2.5 nm s $^{-1}$ at 5°C table temperature. Finally, the residue of the resist was removed by immersing the sample in N-methylpyrrolidone solution heated to 60 °C.

Experimental set-up

A custom-built near-infrared microscope was developed to image the spectral dispersion of the Dirac metasurfaces. Light from a halogen lamp was collimated and focused on the sample surface using a long-working-distance $50\times$ microscope objective (BoliOptics $50\times$, 0.42 numerical aperture). The back focal plane of the objective was imaged in 4f configuration using the combination of a tube lens and a Fourier lens on the entrance slit of the spectrometer (SpectraPro-HRS500, Teledyne Princeton Instruments). The dispersion from a 300 grooves per mm grating was imaged by a near-infrared camera (NIT HiPe SenS 640) connected to the exit slit of the spectrometer. A paired linear polarizer

and quarter-wave plate were used in the incident optical path for the circular polarization studies. For the real-space imaging of the Dirac waveguide modes, we used a laser beam with a linewidth of 5 nm. The laser beam was generated by a supercontinuum light-source (Leukos Electro-VIS) connected to an acousto-optical tunable filter (Leukos Tango-NIR2). A telescope was built into the incident beam optical path with an aperture (25 μ m) in the k-space position of the first lens. The selective wavevector (k) excitation was performed by translating the aperture along the $k_{\rm y}$ direction of the k-space to couple a specific waveguide mode. Images of the real-space propagation of the excited Dirac waveguide mode were captured by the near-infrared camera.

Data availability

The data that support the findings of this study are available from the corresponding author upon reasonable request.

Acknowledgements

The work was supported by the Office of Naval Research (ONR) award N00014-21-1-2092 (A.B.K.), the National Science Foundation (NSF) grant DMR-1809915 (A.B.K.) and the Simons Collaboration on Extreme Wave Phenomena (A.B.K.). D.S. acknowledges support from the Australian Research Council (DE190100430). J.A. and M.A. thank AFRL/RW Emerging Technologies for their support. Fabrication of samples for this work was performed at the Nanofabrication Facility at the Advanced Science Research Center at The Graduate Center of the City University of New York.

Author contributions

A.B.K. conceived the research. D.S. performed theoretical calculations. S.K. and A.V. performed first-principles simulations, fabrication of samples and optical characterization, including real-space imaging and angle-resolved reflectivity measurements. A.V., S.G. and F.K. assembled the experimental set-up. A.B.K., M.A. and J.A. guided and supervised the project. All authors contributed to discussion of the results and manuscript preparation.

Competing interests

The authors declare no competing interests.

Additional information

Supplementary information The online version contains supplementary material available at https://doi.org/10.1038/s41565-023-01380-9.

Correspondence and requests for materials should be addressed to Alexander B. Khanikaev.

Peer review information *Nature Nanotechnology* thanks Baile Zhang and the other, anonymous, reviewer(s) for their contribution to the peer review of this work.

Reprints and permissions information is available at www.nature.com/reprints.